Front. Earth Sci. 2022, 16(2): 381–400
https://doi.org/10.1007/s11707-021-0909-6

RESEARCH ARTICLE

Comparing the performances of WRF QPF and PERSIANN-CCS QPEs in karst flood simulation and forecasting by coupling the Karst-Liuxihe model

Ji LI (✉)[1,2], Daoxian YUAN[1,2], Yuchuan SUN[1], Jianhong LI[2]

1 Chongqing Jinfo Mountain Karst Ecosystem National Observation and Research Station, School of Geographical Sciences, Southwest University, Chongqing 400715, China
2 Key Laboratory of Karst Dynamics (MNR & Guangxi) Institute of Karst Geology, CAGS, Guilin 541004, China

Abstract Long-term rainfall data are crucial for flood simulations and forecasting in karst regions. However, in karst areas, there is often a lack of suitable precipitation data available to build distributed hydrological models to forecast karst floods. Quantitative precipitation forecasts (QPFs) and estimates (QPEs) could provide rational methods to acquire the available precipitation data for karst areas. Furthermore, coupling a physically based hydrological model with QPFs and QPEs could greatly enhance the performance and extend the lead time of flood forecasting in karst areas. This study served two main purposes. One purpose was to compare the performance of the Weather Research and Forecasting (WRF) QPFs with that of the Precipitation Estimations through Remotely Sensed Information based on the Artificial Neural Network-Cloud Classification System (PERSIANN-CCS) QPEs in rainfall forecasting in karst river basins. The other purpose was to test the feasibility and effective application of karst flood simulation and forecasting by coupling the WRF and PERSIANN models with the Karst-Liuxihe model. The rainfall forecasting results showed that the precipitation distributions of the 2 weather models were very similar to the observed rainfall results. However, the precipitation amounts forecasted by WRF QPF were larger than those measured by the rain gauges, while the quantities forecasted by the PERSIANN-CCS QPEs were smaller. A postprocessing algorithm was proposed in this paper to correct the rainfall estimates produced by the two weather models. The flood simulations achieved based on the postprocessed WRF QPF and PERSIANN-CCS QPEs coupled with the Karst-Liuxihe model were much improved over previous results. In particular, coupling the postprocessed WRF QPF with the Karst-Liuxihe model could greatly extend the lead time of flood forecasting, and a maximum lead time of 96 h is adequate for flood warnings and emergency responses, which is extremely important in flood simulations and forecasting.

Keywords WRF QPF, PERSIANN-CCS QPEs, the Karst-Liuxihe model, flood simulation and forecasting, karst river basin

1 Introduction

In karst areas, the general lack of long-term weather data, especially precipitation data, is a great challenge in the simulation and forecasting of flood events based on hydrological models (Li et al., 2019). Especially in the upstream areas of basins, which comprise mountains and valleys with complex topographies, it is difficult to set up rain gauges to effectively obtain rainfall data. Taking the study area in this paper as an example, i.e., the Liujiang karst basin in south China, the drainage area is 5.8×10^4 km^2. However, there are only 66 rain gauges. On average, there is only approximately 1 rain gauge per 1000 km^2, and the representativeness is too weak to reflect the actual rainfall that occurs in the basin. Under these circumstances, effective precipitation results could potentially be acquired by using numerical weather models in karst river basins. Quantitative precipitation forecasts and estimates (QPFs and QPEs, respectively) may enable precipitation data in karst river basins to be easily obtained (Li et al., 2017, 2019).

In recent years, numerical weather prediction models have become increasingly mature with the considerable

Received November 17, 2020; accepted May 26, 2021

E-mail: 445776649@qq.com

progress of 3S (remote sensing (RS), geographic information system (GIS), and global positioning system (GPS)) technologies and can provide a global range of rainfall forecasting products with high precision. The current mainstream numerical weather models include the European Centre Weather Forecasts model (Molteni et al., 1996), the Japan Meteorological Agency meteorological model (Takenaka et al., 2011), the QPEs by weather radars (Delrieu et al., 2014; Rafieei et al., 2014; Faure et al., 2015), WRF QPF (Skamarock et al., 2008; Zaripov et al., 2016; Yáñezmorroni et al., 2018), satellite QPEs (Bartsotas et al., 2017; Wardhana et al., 2017), and others. Among these weather models, WRF QPF and PERSIANN-CCS QPEs may be most effective for acquiring precipitation results in karst basins (Soroosh et al., 2000; Yang et al., 2004, 2007; Skamarock et al., 2008).

Studies of the WRF model in karst areas usually focus on precision and uncertainty analysis of the model in predicting rainfall. Among these studies, many focus on the uncertainty analysis of WRF model parameters for different karst landforms. Leeper et al. (2011) studied the outputs of WRF model parameter scheme adjustment on the rainfall forecast results in karst areas, especially the influence of the karst landscape on the parameter scheme. Johnson (2014) studied the influence of karst landscapes on weather systems based on the WRF model, for which the response processes of the model to different land use patterns and soil types were calculated. Johnson et al. (2017) assessed the uncertainty of the WRF model corresponding to land use changes and different soil conditions. Lahmers (2017) improved the structure of the WRF-Hydro Hydrologic Model so that it could be used to simulate hydrological processes in semiarid areas. In karst areas, the current WRF QPF model can provide rainfall forecast results with a long lead time (Li et al., 2015; Li et al., 2017). The lead time of the QPF produced by the latest WRF model is 1–15 days (Ahlgrimm et al., 2016). Therefore, coupling hydrological models with WRF QPFs for flood warning and forecasting in karst areas can greatly extend the lead time (Zappa et al., 2010), which is very important for flood warnings and mitigation because more time is provided for flood emergency responses (Tingsanchali, 2012). However, the current mainstream WRF QPF models can only guarantee satisfactory rainfall prediction accuracy within the forecast period of 24 h (Leeper et al., 2011; Johnson, 2014; Li et al., 2017, 2019). In this study, the maximum lead time of the WRF QPF is 96 h. This is the equivalent of a 96 h forecast period of flood forecasting in karst basins, which is very important for the safe evacuation of people and property before floods and is the greatest factor of concern for decision makers in flood forecasting.

PERSIANN-CCS is a QPE technology produced by weather satellites that can estimate long-term and high-resolution rainfall data (Yang et al., 2004, 2007). In current QPE technology research, many studies have been conducted on the PERSIANN prototype system (Hsu et al., 1999; Soroosh et al., 2000; Yang et al., 2007; Hsu et al., 2008) and its subsystem, the PERSIANN-Climate Data Record (CDR) (Higgins et al., 2007; Mekonnen and Hossain, 2010; Hu et al., 2013; Nguyen et al., 2017). However, only a few studies coupling PERSIANN-Cloud Classification System (CCS) QPEs with a distributed hydrological model in karst areas have been conducted (Stenz, 2014; Li et al., 2019).

Some studies have been performed on coupling the PERSIANN prototype system with a distributed hydrological model. For instance, Bitew and Gebremichael (2011) studied the coupling outputs of the PERSIANN model with the MIKE SHE hydrologic model in a medium-sized (1656 km^2) mountainous watershed in the Ethiopian highlands and evaluated satellite rainfall products. Gebregiorgis and Hossain (2013) assessed the uncertainty of PERSIANN satellite rainfall results and reported that rainfall estimations by the PERSIANN system provide meaningful guidance for improving algorithms to advance hydrologic prediction. In their study, the uncertainties of three satellite rainfall products were explored for five regions of the Mississippi River basin. The results showed that satellite rainfall uncertainty was dependent more on topography than on the climate of the region. The terrain in karst areas is usually highly complicated, so there may be some deviation in satellite rainfall estimations by the PERSIANN system. Therefore, this paper intended to test the feasibility of PERSIANN-CCS QPEs by applying them in karst areas.

A distributed hydrological model, as a physics-mathematics computational tool, is an important method used to accurately simulate and forecast flood events in karst basins (Shuster and White, 1971; Ford and Williams, 1989; White, 2002, 2007; Scanlon et al., 2003). Precipitation, as the input data for hydrological models, could be the driving factor in flood forecasting (Li et al., 2017). Coupling a distributed hydrological model with WRF QPF and PERSIANN-CCS QPEs has great capacity and prospects for flood simulations and forecasting in karst areas. The entire karst basin can be divided into many grid units known as karst subbasins by digital elevation model (DEM) data in distributed models (Kovacs and Perrochet, 2011; Chapuis et al., 2020), and the actual karst development characteristics and rainfall-runoff processes can be precisely reflected by coupling high-resolution grid rainfall with WRF QPF and PERSIANN-CCS QPEs.

In this study, a new generation of physically based distributed hydrological models for watershed flood simulation and forecasting, i.e., the Karst-Liuxihe model (Li et al., 2019), was employed to couple WRF QPF and PERSIANN-CCS QPEs for application in karst areas. The Karst-Liuxihe model was improved by adding the karst mechanism based on the Liuxihe model prototype (Chen, 2009, 2018; Chen et al., 2015, 2016, 2017). The underground structure of the Liuxihe model was an integral

structure with only 1 layer (Fan et al., 2012; Chen et al., 2016; Li et al., 2017). The linear reservoir method was used to calculate the confluence of underground runoff (Chen et al., 2015; Hui et al., 2015; Li et al., 2017, 2019), which was not suitable for multilayer and nonlinear karst groundwater confluences. Therefore, Li et al. (2019) improved the structure and function of the original Liuxihe model. In particular, the calculation module of subsurface runoff confluence was redesigned, and the calculation of water transport and transformation in the key karst zone was added, which made the Karst-Liuxihe model suitable for flood simulation and forecasting in karst areas.

It should be pointed out that the previous application of this Karst-Liuxihe model in karst areas was based on rainfall data observed by rain gauges, and it was not clear whether it was suitable for coupling with numerical weather models in karst basins. The coupling of weather models and hydrological models will inevitably lead to the problem of superposition of system errors, resulting in the uncertainty of the final simulation results. In the present study, a sensitivity analysis was conducted for the parameters of the coupled model, i.e., coupling WRF QPF and PERSIANN-CCS QPEs with the Karst-Liuxihe model, to determine the sensitivity of each parameter in flood simulations. This study focused on 1) whether this coupled model was applicable to karst areas and 2) how to revise the rainfall results produced by the two weather models. A postprocessing algorithm was proposed to correct the WRF QPF and PERSIANN-CCS QPE results in karst areas, which could reduce rainfall uncertainties and make the results easier to understand and more credible.

2 Study area and data set

2.1 Study area

The Liujiang karst river basin, the most developed karst basin in southwest China, is selected as the study area (23.9°N–24.5°N, 108.9°E–109.7°E). The basin area is approximately 5.78×10^4 km^2. The average annual precipitation is 1400–1700 mm. The flood season is from May to September, and the flood volume can account for 80% of the total runoff. In the upper reaches, most of the landforms were deep-cut V-shaped canyons, except in the headwaters. The elevation of these canyons is usually greater than 1000 m, with relative heights of 500–700 m. In these canyons, the runoff responds quickly to rainfall, and the area is prone to regional flood disasters. Figure 1 shows a sketch map of the study area.

The upstream area of the basin is located in the southern part of the ancient Palaeocaledonian fold belt and in the south-eastern edge of the southwest China depositional area, where a large area of sedimentary rock is distributed. The outcrop strata in the basin are ancient and intact and mainly include Sinian, Cambrian, Silurian, Ordovician, Upper Devonian, Lower Carboniferous, Upper Permian, Lower Triassic, Palaeogene, Quaternary Pleistocene and Holocene strata.

After a long karst landform evolutionary process, karst development in the basin is now very mature. At first, there were mainly small karst doline funnels in the basin. Then, the landform evolved into a peak cluster depression (Fig. 2) as carbonate rocks continued to be eroded by karst water as well as the fluviraption of allogeneic water, especially from the Liujiang River. Under these interior erosional outputs and exterior fluviraption for many years, the geomorphological evolution matured, i.e., the peak cluster depressions evolved into peak forests (Williams, 1978), especially in the downstream area.

In the 1990s, the frequency and intensity of rainstorms and flood disasters increased with the increase in extreme weather in the study area (Li et al., 2017). The north-eastern and western areas of the basin are the main flood sources, and this is the area where the most developed karst is located. In particular, karst conduits are well developed in underground aquifers (Li et al., 2019). The karst features can significantly affect the hydrologic process, especially during the rainfall-runoff process in the model. It is highly challenging to accurately simulate karst water cycle rules and to forecast flood changing trends.

2.2 Rainfall, flood and property data

In the study area, the flood characteristics are closely related to rainstorms, the watershed topography and the karst landforms. Larger floods are mostly multipeak processes, and the most intense flooding lasts only a short period of time, i.e., the flood peak occurs quickly and recedes quickly, which usually causes considerable damage. According to the tracing test conducted in the study area, the flood flow rate is approximately 43.2–129.6 km/d during the flood period. The extreme flow rate can reach 172.8 km/d, which indicates that the karst conduit is well developed underground. Karst features can significantly affect the flood process, especially during the rainfall-runoff process.

In the study area, there are a total of 66 rain gauges and 156 grid points for WRF QPF and 131 grid points for PERSIANN-CCS QPEs (as shown in Fig. 1(a)). The rainfall outputs from these 3 sources, i.e., observed rainfall by rain gauges, WRF QPF and PERSIANN-CCS QPEs, were input into the Karst-Liuxihe model for flood simulations. Simulation results based on the coupled model were investigated to evaluate the performance of the coupled model. In total, 20 flood events (from June, 1994 to June, 2013) that occurred in the study area were simulated. Among these floods, the first four were used to calibrate the model parameters, and the remaining floods were used to validate the model outputs. Key input data to the coupled model include DEM data (Fig. 1(b)), land use (Fig. 1(c)) types, and soil types (Fig. 1(d)). These property

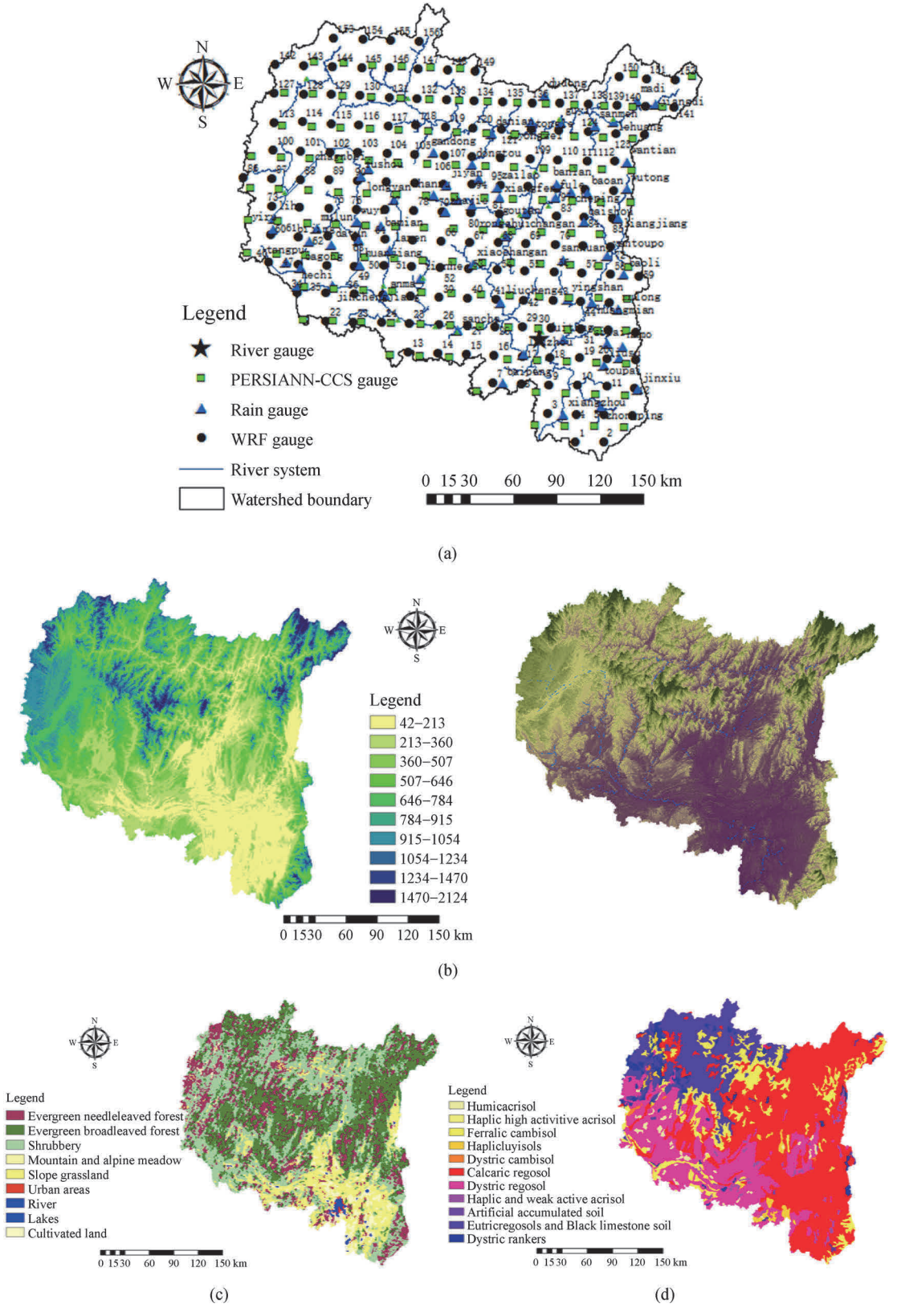

Fig. 1 Sketch image of the Liujiang watershed. (a) Gauge distribution (modified from Yang et al., 2008); (b) the DEM image; (c) land use types; (d) soil types.

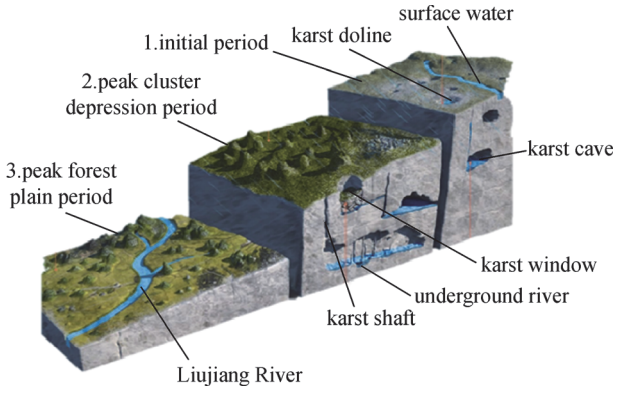

Fig. 2 The karst landform evolution of the Liujiang Basin (modified from Zheng and Lan, 2019).

data can be downloaded easily from the internet without cost (the names of websites are provided at the end of this article). It should be noted that the spatial resolution of these original DEM, land use, and soil type data must be consistent with the resolution of the two weather models in this study. The original resolutions of the DEM, land use, and soil type data were 90 m × 90 m, 1000 m × 1000 m, and 1000 m × 1000 m, respectively. The data sets were resampled to 200 m × 200 m to match the resolution of the two weather models used in this study.

3 Methods

3.1 WRF QPF

The WRF QPF used in this study was the WRF Advanced Research model version 3.4 (Skamarock et al., 2008), which is a 3-dimensional and nonhydrostatic system that can effectively forecast complex weather changes on the cloud scale and synoptic scale. This model is especially precise at horizontal resolutions of 1–10 km, which can satisfy the practical application requirements of rainfall forecasting in this study. WRF QPF was applied in this study using the following configurations. 1) The domain of the WRF QPF model was set at 24°N and 109°E, as the location of the basin is 23.9°N–24.5°N, 108.9°E–109.7°E. 2) The vertical structure of the model included 28 levels with the Lambert conformal projection (Li et al., 2015). 3) The initial temporal and spatial resolutions were 3 h and 0.5°, respectively, at horizontal resolution. Following downscaling, the temporal and spatial resolutions were 1 h and 200 m × 200 m, respectively. The downscaling method was calculated in ArcGIS 10.2 using the statistical scale relationship between the DEM data and the weather model (Fan et al., 2017). 4) The entire basin was covered by 156 grid gauges based on the WRF QPF. Rainfall forecasting was produced with a lead time of 96 h (the results of other lead times, such as 24, 48, and 72 h, were also calculated (Li et al., 2017)). 5) The WRF QPF results were evaluated and revised by comparison to the rainfall data from the rain gauges.

The WRF QPF parameters were set according to the following configurations. 1) The single-moment, 3-class microphysics parameterization was used in this study (Hong and Lim, 2006). 2) The Yonsei University (YSU) planetary boundary layer scheme and the Kain-Fritsch cumulus parameterization (Kain, 2004) were adopted to optimize the cumulus parameters. 3) Other physics schemes for the model parameters used in this paper included the Goddard scheme (Chou and Suarez, 1994), rapid radiative transfer model (Mlawer et al., 1997) and NOAH scheme (Ek et al., 2003). More details on the WRF QPF model and its parameter settings can be found in the research results of previous studies (Li et al., 2015; Li et al., 2017).

3.2 PERSIANN-CCS QPEs

The PERSIANN-CCS QPEs (Yang et al., 2004, 2007), which were developed based on the PERSIANN prototype system (Hsu et al., 1999), are a next-generation rainfall estimation system based on geostationary satellites that use computer imaging technology and pattern recognition technology. The PERSIANN-CCS QPE system was based on geostationary infrared imagery and daytime visible imagery (Soroosh et al., 2000). The system is automated for estimating precipitation through the use of satellite remote sensing technology. The parameters of the PERSIANN system can be optimized efficiently by a self-adaptive artificial neural network (Yang et al., 2007).

The model setup, parameter optimization and rainfall estimation procedures of the PERSIANN-CCS (Li et al., 2017) can be found in operating manuals and user guides (available at CHRS website). In fact, in practical applications, there is no need to build the PERSIANN-CCS QPE model to estimate rainfall results in a given study area. Worldwide products of QPEs based on the PERSIANN-CCS, including the rainfall results in this paper, can be downloaded without cost from CICS website. Therefore, rainfall data from the PERSIANN-CCS QPEs can be obtained expediently in karst areas, where rain gauges are usually lacking.

The specific operational steps for the PERSIANN-CCS QPEs in this study area were as follows. 1) The time and scope of the study area, i.e., the rainfall occurrence and end time, as well as the location according to the longitude and latitude, were determined. 2) The estimated precipitation data produced by the PERSIANN-CCS were downloaded. 3) The products of the PERSIANN-CCS QPEs were analyzed and appraised by comparison to the rainfall observed by rain gauges. 4) The PERSIANN-CCS QPE products were revised using appropriate methods.

The PERSIANN-CCS QPE products can generate precipitation data at a time interval of 30 min and a spatial resolution of 0.04° × 0.04° (Yang et al., 2007). The spatial

resolution was upscaled to 200 m × 200 m using a downscaling method (Fan et al., 2017) to suit the resolution of the Karst-Liuxihe model in this paper. The time interval was changed to 1 h.

3.3 Postprocessing of the 2 weather models

It should be noted that a certain degree of uncertainty remains, and it cannot be neglected in the model application of WRF QPF and PERSIANN-CCS QPEs. This uncertainty is mainly associated with the systematic errors of the model itself (Moradkhani et al., 2006; Bartsotas et al., 2017), which result in poor precision of the rainfall results (Goudenhoofdt and Delobbe, 2009; Kai et al., 2014; Wardhana et al., 2017). The rain gauge precipitation can directly reflect the actual rainfall situation in the basin, which is the reason why the rain gauge precipitation taken as the true value was used to calibrate the 2 weather models in this paper.

To make the quantitative values of the rainfall results from the WRF QPF and PERSIANN-CCS QPEs closer to those of the precipitation observed by the adjacent rain gauges, which would make the forecasting rainfall results more credible, the precipitation products produced by the 2 weather models were revised using the adjacent rain gauge precipitation that was considered the true precipitation of the basin. The postprocessing procedures of the 2 precipitation products were as follows.

1. The average values of the WRF QPF and PERSIANN-CCS QPEs were calculated according to the following equation:

$$\overline{P}_{\text{WRF/PERSIANN-CCS}} = \frac{\sum_{i=1}^{N} P_i F_i}{A \times N}, \tag{1}$$

where $\overline{P}_{\text{WRF/PERSIANN-CCS}}$ indicates the average values of the precipitation results based on the WRF QPF and PERSIANN-CCS QPEs, mm; P_i is the precipitation of the 2 weather models at grid gauge i, mm; F_i is the watershed area of grid gauge i, mm^2; A is the basin area, mm^2; and N is the number of grid gauges.

2. The average values of the observed precipitation based on rain gauges were determined by the following equation:

$$\overline{P}_2 = \frac{\sum_{j=1}^{M} P_j}{M}, \tag{2}$$

where $\overline{P}_2$ is the average value of the rain gauge precipitation, mm; M is the number of rain gauges; and P_j is the average value of the precipitation observed by the j rain gauge, mm.

3. Average values of the rain gauge precipitation were adopted to correct the WRF QPF and PERSIANN-CCS QPEs using the following equation:

$$P_i^{'} = P_i \times \frac{\overline{P}_2}{\overline{P}_{\text{WRF/PERSIANN-CCS}}}, \tag{3}$$

where $P_i^{'}$ is the quantitative value of the precipitation according to the WRF QPF and PERSIANN-CCS QPEs after revision at grid gauge i, mm, and P_i indicates the precipitation values of the 2 weather models at grid gauge i, mm.

This postprocessing method made the rainfall results based on the PERSIANN-CCS QPEs and WRF QPF closer to the observed rainfall results produced by rain gauges, which can largely reduce the systematic errors of the weather models (Li et al., 2019). After postprocessing, the precipitation products based on the 2 weather models were fed into the Karst-Liuxihe model to validate the feasibility of this postprocessing method in karst flood event simulation and forecasting in the study area.

3.4 The Karst-Liuxihe model

The Liuxihe model, a terrestrial hydrological model, was proposed by Chen (2009) and has achieved many reasonable research results in forecasting surface rivers (Chen, 2009, 2018; Chen et al., 2016, 2017; Li et al., 2017, 2019). However, this model may not be applicable to the study of karst hydrology simulations. The main reasons are as follows: 1) in the model structure design, the Liuxihe model was intended to treat the underground layer as a whole (Li et al., 2017, 2019), and the calculation of the underground water-bearing system was not further stratified. However, karst water-bearing systems have a complex, multilevel, and anisotropic spatial structure. Therefore, this model is not applicable to karst areas in terms of structural mechanisms. 2) In terms of the model algorithm, the groundwater runoff confluence of the Liuxihe model runoff adopted a linear reservoir method (Chen et al., 2016), which did not consider the behavior of water transport and transformation in the complex and nonlinear karst water-bearing medium.

To be suitable for karst hydrology simulation, the structure of the Liuxihe model should be improved to effectively adapt to the complex karst hydrogeological conditions, which involves adding the karst mechanism to the model. Li et al. (2019) developed the Karst-Liuxihe model by improving the model structure and algorithm based on the prototype of the Liuxihe model, which made the improved Karst-Liuxihe model suitable to simulate flood events in karst areas. The processes of improving the structure for the original Liuxihe model and developing the Karst-Liuxihe model are summarized as follows (Li et al., 2019): 1) simplifying the karst water-bearing media in the model; 2) refining the smallest calculation unit of the karst

basin; 3) improving the calculation of water movement rules in karst aquifers; and 4) adding some necessary hydrogeological parameters to the model.

The Karst-Liuxihe model generated good results in several karst basins, which indicated that it was suitable in karst basins (Li et al., 2019, 2020, 2021). Therefore, this Karst-Liuxihe model was adopted to simulate and forecast karst flood events in this study.

4 Coupled model setup

4.1 Model initial condition setting

Initial conditions need to be set before the model can simulate floods, such as depression detention and soil moisture before flooding. When the Karst-Liuxihe model was applied in karst areas, we focused on the output of pits (sinks) in karst topography, such as depressions, on the flood propagation process. This emphasis had a great influence on the flood forecast results.

In general, there are many pits in karst areas, some of which are false pits. The existence of false pits is due to incorrect data and systematic errors of the DEM itself. These false pits need to be reasonably filled before building the coupled model. Because there are karst depressions and sinkholes in karst areas, which cause true pits to exist, the model retained these true pits, including depressions and sinkholes. These true pits in the study area play an important role in the flood routing process. Due to the detention output and peak clipping in karst depressions, the hydrological process is delayed, especially the flood peak flow (Li et al., 2019). Before building the model, whether there exists a detention output or peak clipping in the karst depressions and sinkholes in the study area is a key factor. If so, the storage capacity and size of these pits can be determined by a field survey during floods. The capacity can be deduced according to the water level, and the amounts of flood detention near the pits must be considered in the water balance calculation in the model. This information can improve the accuracy of the model in karst flood event simulation and forecasting.

The specific calculation steps to determine whether there is a flood detention output or peak clipping were as follows.

First, the limit discharge capacity of the underground river entrance in the study area, i.e., Q_{max}, was deduced through a field investigation and monitoring.

Then, the water inflow from the entrance of the underground river, i.e., Q_{in}, could be calculated using the coupled model. The relationship between Q_{in} and Q_{max} was compared to determine whether the flood detention phenomenon was generated.

If $Q_{in} > Q_{max}$, the flood detention phenomenon was generated, and then the flow of the underground river outlet, $Q_{out} = Q_{max}$, was generated. The water storage of the flood detention from the entrance of the underground river, Q_s, was as follows:

$$Q_s = Q_{s1} + Q_{in} - Q_{max}, \tag{4}$$

where Q_s is the water storage of the flood detention during this period, $m^3 \cdot s^{-1}$; Q_{s1} is the water storage of the flood detention from the preceding time period, $m^3 \cdot s^{-1}$; and if there is no flood detention, $Q_{s1} = 0$.

If $Q_{in} \leqslant Q_{max}$ and $Q_{s1} = 0$, then

$$Q_{out} = Q_{in}. \tag{5}$$

If $Q_{in} \leqslant Q_{max}$, $Q_{s1} > 0$ and $Q_{in} + Q_{s1} \leqslant Q_{max}$, then

$$Q_{out} = Q_{in} + Q_{s1}. \tag{6}$$

Otherwise, if $Q_{in} \leqslant Q_{max}$, $Q_{s1} > 0$ and $Q_{in} + Q_{s1} > Q_{max}$, then

$$Q_{out} = Q_{max}. \tag{7}$$

For the model setup, the initial values for some parameters need to be determined. For instance, the initial soil moisture was set to [0%, 100%], with 0 indicating extremely dry soil and 100 indicating saturated soil water content. After running the model calculations 100 times, the appropriate initial water content of the soil was determined according to the outputs of flood simulations. Based on the 20 flood simulation tests by the Karst-Liuxihe model in this study area, the initial soil moisture was usually 50%–80% of the saturated soil moisture during floods. The soil water content before each flood is different and needs to be determined by trial model calculations. In multiple successive flood forecasts, the soil moisture content during the previous flood recession can be used as the soil moisture at the beginning of the next flood event; if the time interval between the two floods is long, the soil moisture content at the beginning of the next flood needs to be estimated based on the soil moisture after the last flood and the calculated amount of evapotranspiration in the basin.

4.2 Parameter optimization

The optimization of hydrological model parameters based on historical rainfall and flow data in the study area is very important for subsequent flood simulation and forecasting, which is equivalent to an essential training process for the application of hydrological models to describe the local hydrological cycle (Chen, 2009, 2018). To verify the necessity of parameter optimization for the coupling model, the flood simulation outputs by the initial model parameters and those after parameter optimization were compared. Table 1 lists the ranges of the initial hydrogeological parameters and rainfall infiltration coefficients.

There are 20 parameters in the Karst-Liuxihe model, and 18 require calibration (Li et al., 2019), for which an

Table 1 Initial hydrogeological parameters

(a) Initial parameter value range of the epikarst zone

Thickness (h)/m	Saturated water content (θ_{sat})/(g·cm^{-3})	Saturation permeability coefficient (θ_s)/(mm·h^{-1})	Karst fissure width (wd)/cm	Macro crack volume ratio (V)/%	Field capacity (θ_{fc})/mm
2.5–8	0.15–0.3.5	110–400	0.1–10	0.08–0.25	0.26–0.48

(b) The rainfall infiltration coefficient for different karst development characteristics

Landforms	Karst strongly developed	Karst moderately developed	Karst poorly developed
Closed depression	0.62–0.85	0.45–0.65	0.15–0.18
Not closed depression	0.34–0.67	0.32–0.55	0.18–0.28
Monadnock, platform	0.25–0.35	0.22–0.35	0.20–0.25
Gully, slope	0.01–0.25	0.01–0.24	0.01–0.25

improved particle swarm optimization (PSO) algorithm, mainly involving improvements to the algorithm parameters, was produced to improve the performance and convergence efficiency (Chen et al., 2016). Before parameter optimization by the improved PSO algorithm, some initial conditions need to be determined as follows:

1) The number of particles of the improved PSO algorithm was set to 20, and the maximum number of iterations was set to 1000.

2) The convergence accuracy of iterative calculations was 10^{-4}.

3) Three parameters were included in the PSO algorithm: the inertia weight ω and the self and group learning acceleration coefficients C1 and C2, respectively. The initial value range of inertia weight ω was set from 0.1 to 0.9, and the value range of the acceleration coefficient was set to 1.25 to 2.75 for C1 and 0.5 to 2.5 for C2.

In the study area, 20 floods from 1994 to 2013 were used to validate the Karst-Liuxihe model performance in karst flood simulations. Four floods were used for parameter optimization, and the best flood simulation was adopted for the final parameter calibration.

4.3 Parameter sensitivity analysis

A multiparameter sensitivity analysis (Choi et al., 1999) was used to analyze the sensitivity of the coupled model parameters in this study, for which the Nash–Sutcliffe coefficient was used as the objective function:

$$NSC = 1 - \frac{\sum_{i=1}^{n} (Q_i - Q_i')^2}{\sum_{i=1}^{n} (Q_i - \overline{Q})^2}, \quad (8)$$

where NSC is the value of the objective function, i.e., the Nash–Sutcliffe coefficient/C; Q_i and Q_i' are the observed and simulated water flows, respectively, m^3·s^{-1}; $\overline{Q}$ is the average observed water flow value, m^3·s^{-1}; and n is the observed period number, hours.

The steps of parameter sensitivity analysis were as follows:

1) Initial conditions setup: the initial value range of the parameter was set to [0.4, 3.2] based on the parameter properties; the convergence precision was 10^{-4}; and the threshold value of the Nash coefficient was set to 80%.

2) Sampling method: the Monte Carlo sampling method was used to sample the parameter sets, for which 8000 sets of parameter sequences were obtained.

3) Flood simulations: the above parameter sequences were input into the Karst-Liuxihe model to simulate the floods, and the Nash coefficient of each simulation was recorded.

4) Effect appraisal: the Nash coefficient was compared with the threshold of 80%. If it was less than 80%, it was an unacceptable value; otherwise, it was an acceptable value.

5) Parameter sensitivity calculation: the degree of separation was assessed between acceptable and unacceptable values, which represented the sensitivity of each parameter. This degree of separation (*DS-NSC*) was calculated according to Eq. (8).

A flow chart of the parameter sensitivity analysis is shown in Fig.3.

5 Results

5.1 Precipitation results from WRF and PERSIANN-CCS

There are 156 grid gauges for WRF QPF and 131 grid gauges for PERSIANN-CCS QPEs in this study area. These grid gauges can cover the entire basin (as shown in Fig. 1(a)) and provide a representative rainfall product. The WRF QPF model offered rainfall forecasting with a lead time of 96 h, whereas the rainfall estimation results of PERSIANN-CCS had no lead time. The hourly precipitation data for 2008, 2009, 2011, 2012, and 2013 from the products of the 2 weather models were produced, compared, and revised in this study using the observed precipitation data from rain gauges. The forecasting,

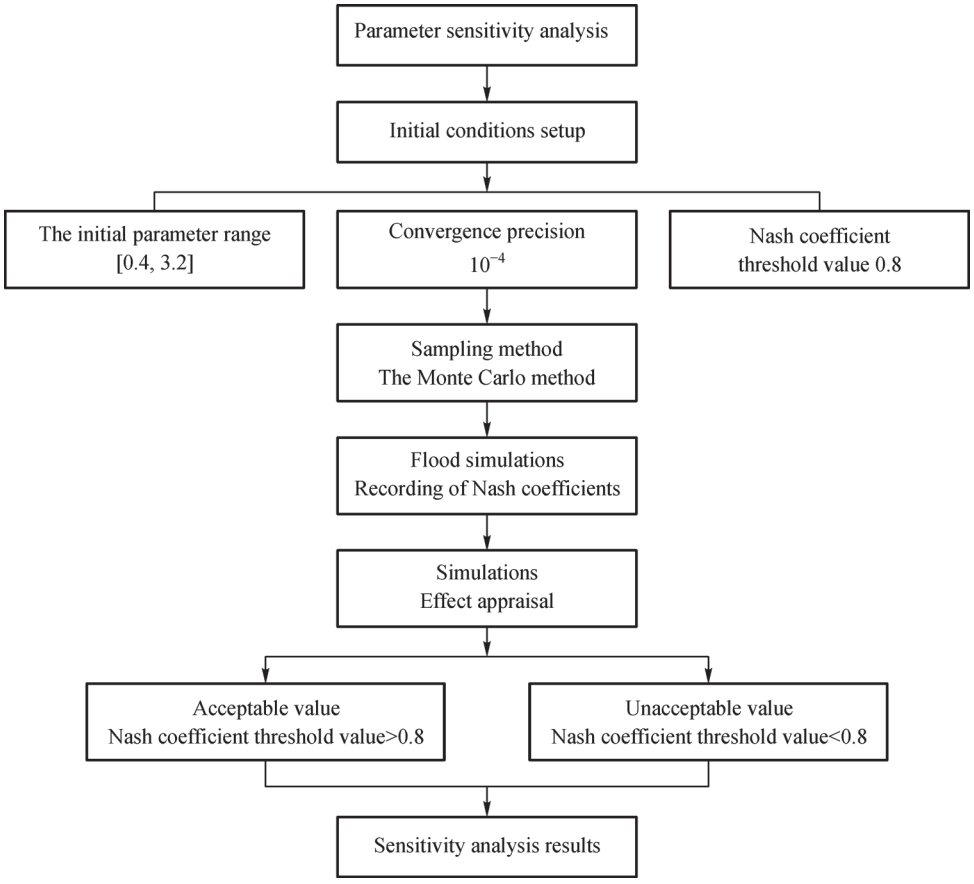

Fig. 3 The flow chart of the parameter sensitivity analysis.

estimation, and comparison of the rainfall results produced by the 3 precipitation products, i.e., the WRF QPF model, PERSIANN-CCS QPEs and rain gauge precipitation, are shown in Fig. 4.

Figure 4 shows the average value of the rainfall results of the WRF QPF model, PERSIANN-CCS QPEs, and the rain gauge precipitation, where Figs. 4(a), 4(b), and 4(c) are the average rainfall of the unit area by the rain gauge, WRF QPF, and PERSIANN-CCS QPEs, respectively (the *x*-axis is rainfall duration, hours, and *y*-axis is the average rainfall of the unit area, mm); Fig. 4(d) and Fig. 4(e) are the quantile-quantile plots in which a 45° line is drawn to compare the rainfall results of the 2 weather models and the rain gauge precipitation, respectively; and Fig. 4 is the rainfall results of 2008, 2009, 2011, 2012, and 2013, respectively.

According to the results shown in Fig. 4, the rainfall distributions of WRF QPF, PERSIANN-CCS QPEs, and observed precipitation data appear to be quite similar. In particular, according to Figs. 4(d) and 4(e), the 2 precipitation plots, i.e., WRF QPF relative to the rain gauge precipitation and PERSIANN-CCS QPEs relative to the rain gauge precipitation, were very closely distributed around the 45° lines, and the correlation coefficients (R^2) were all above 0.9 (Figs. 4(d) and 4(e)), meaning that the distributions of these 3 rainfall products were close to one another. However, the relative errors of the 3 rainfall products cannot be ignored. The results from WRF QPF were larger than those from the rain gauges, while those of PERSIANN-CCS QPEs were smaller, which showed that relative errors existed between the weather model precipitation values and the rain gauge precipitation.

5.2 Results of the parameter optimization for the coupled model

An improved PSO algorithm (Chen et al., 2016) was used to optimize the model parameters. The floods 2005-06-14-06:00, 2006-06-04-12:00, 2007-07-08-10:00, and 2008-06-09-08:00 were used for parameter optimization. To compare the output of parameter optimization, we also compared the output of the model flood simulation based on the initial parameters with that after parameter optimization. These flood simulation outputs through parameter optimization are drawn in Fig. 5. The 6 evaluation indices of the flood simulations, including the Nash–Sutcliffe coefficient (*C*), the coefficient of the water balance (*W*), the correlation coefficient (*R*), the flood peak flow relative error (E%), the process relative error (P%), and the flood peak flow time error (*T*; hours), are listed in

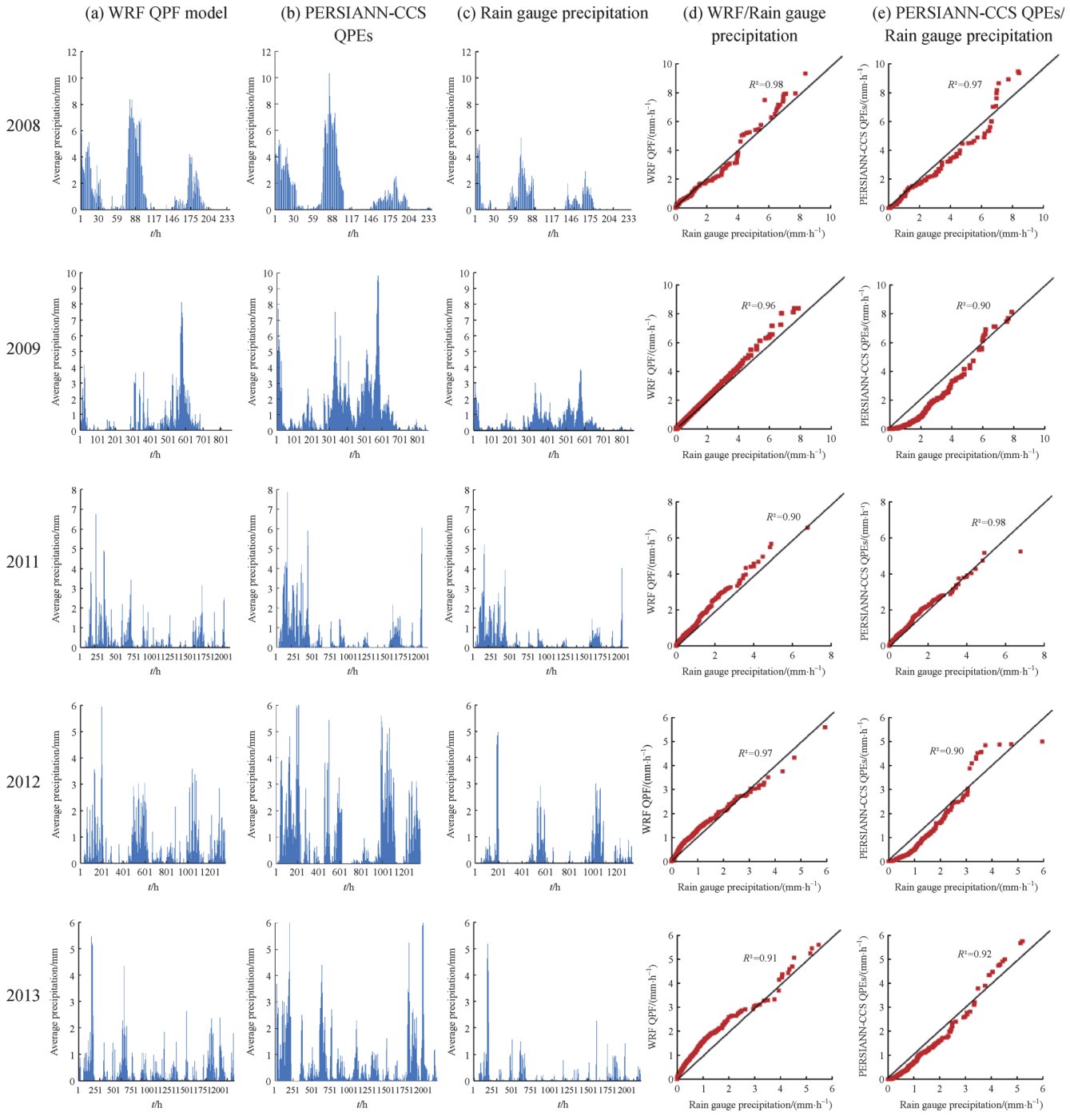

Fig. 4 The rainfall results of the 3 precipitation products.

Table 2.

From Fig. 5, the karst flood outputs simulated through parameter optimization for the coupling model were much better than those simulated by the initial model parameters, especially for the simulated peak flows. Among these flood simulation results, the simulated output of flood 2008-06-09-08:00 was the best, with the simulated flood process closest to the observed process. To further compare the outputs of the flood simulations, 6 evaluation indices, including the Nash–Sutcliffe coefficient, the correlation coefficient, the water balance coefficient, the process relative error, the peak flow relative error, and the peak flow time error, were calculated and are listed in Table 2. The best values of the 6 indices were obtained when modeling flood 2008-06-09-08:00. Therefore, flood 2008-06-09-08:00 was finally used for parameter optimization, and the rest of the flood events were used to validate the model performance.

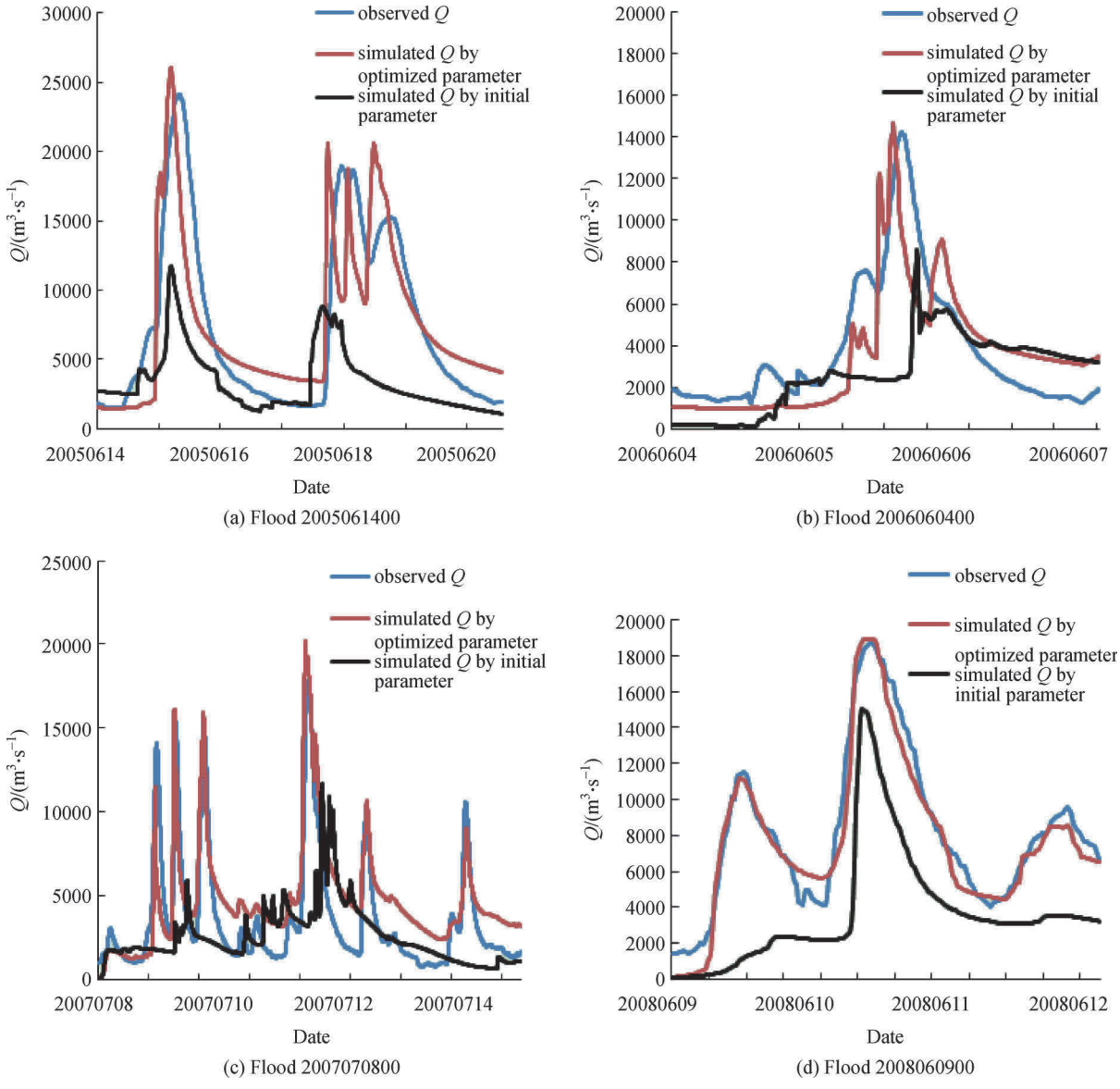

Fig. 5 Karst flood simulation outputs through parameter optimization based on the improved PSO algorithm.

Table 2 shows that the average values of these 6 evaluation indices for flood simulation by parameter optimization in the Karst-Liuxihe model were 0.91, 0.91, 12, 3, 0.92, and −3 h, respectively. For the flood simulation results with the initial model parameters, the values were 0.62, 0.65, 29, 34, 0.69, and −6 h, respectively. Clearly, the model performance in flood simulations was greatly improved after parameter optimization by the improved PSO algorithm. These reasonably simulated flood processes based on the improved PSO algorithm for the Karst-Liuxihe model were well matched to the practically observed values (as shown in Fig. 5 and Table 2), indicating that the improved PSO algorithm was effective and that the Karst-Liuxihe model had a better flood simulation output after parameter optimization than the results achieved using the initial model parameters in karst areas. The results also showed that parameter optimization of the distributed model was necessary and can greatly improve the model performance.

5.3 Flood simulation results by the coupled model

In this study, to analyze the outputs of the karst flood simulation using the initial WRF QPF, PERSIANN-CCS QPEs and their post-processed results, the karst flood events from 2008 to 2013 were simulated by the coupled model. The results comparisons are shown in Fig. 6.

According to Fig. 6, the flood simulations with the original WRF QPF and PERSIANN-CCS QPE products were unsatisfactory, especially for the simulated peak

Table 2 Evaluation indices for the karst flood simulation outputs

Floods	Model parameter types	Nash–Sutcliffe coefficient (C)	Correlation coefficient (R)	Process relative error (P)/%	Peak flow relative error (E)/%	Coefficient of water balance (W)	Peak time error (T)/h
1994060700	Initial	0.65	0.58	37	32	0.76	−6
	Optimized	0.93	0.87	14	2	0.95	−4
1995052100	Initial	0.58	0.61	35	33	0.57	−5
	Optimized	0.85	0.9	20	3	0.81	−3
1996060600	Initial	0.61	0.62	35	35	0.74	−4
	Optimized	0.9	0.93	18	5	0.86	−5
1997060400	Initial	0.59	0.6	31	34	0.72	−5
	Optimized	0.84	0.95	13	2	0.95	−4
1998051600	Initial	0.62	0.58	25	35	0.76	−5
	Optimized	0.83	0.95	10	2	1.05	−2
1999061700	Initial	0.62	0.55	27	38	0.56	−6
	Optimized	0.89	0.93	15	3	0.8	−5
2000052100	Initial	0.54	0.68	26	31	0.58	−6
	Optimized	0.89	0.89	8	2	0.83	−3
2001051500	Initial	0.6	0.65	26	35	0.65	−5
	Optimized	0.91	0.89	12	2	0.82	−4
2002042600	Initial	0.65	0.68	28	29	0.67	−5
	Optimized	0.86	0.9	14	4	0.87	−2
2003060600	Initial	0.63	0.65	24	26	0.65	−5
	Optimized	0.92	0.85	9	3	0.86	−4
2004070300	Initial	0.58	0.62	25	39	0.67	−6
	Optimized	0.88	0.92	13	4	0.85	−3
2005061400	Initial	0.54	0.65	38	45	0.52	−6
	Optimized	0.87	0.92	10	3	1.08	−5
2006060400	Initial	0.66	0.71	28	43	0.61	−7
	Optimized	0.91	0.89	11	5	0.92	−5
2007070800	Initial	0.63	0.66	32	38	0.71	−5
	Optimized	0.89	0.93	14	4	1.12	−3
2008060900	Initial	0.65	0.68	29	32	0.67	−5
	Optimized	0.96	0.94	5	3	0.94	−3
2009060908	Initial	0.67	0.61	28	34	0.79	−4
	Optimized	0.95	0.92	17	4	0.9	−2
2010071208	Initial	0.6	0.65	26	36	0.83	−6
	Optimized	0.88	0.91	15	2	0.89	−4
2011060109	Initial	0.65	0.83	25	21	0.89	−5
	Optimized	0.95	0.92	16	3	1.02	−7
2012060220	Initial	0.69	0.54	31	27	0.75	−6
	Optimized	0.93	0.91	8	5	0.89	−6
2013060114	Initial	0.7	0.84	28	38	0.79	−5
	Optimized	0.95	0.94	7	6	0.92	−4
average value	Initial	0.62	0.65	29	34	0.69	−6
	Optimized	0.91	0.91	12	3	0.92	−3

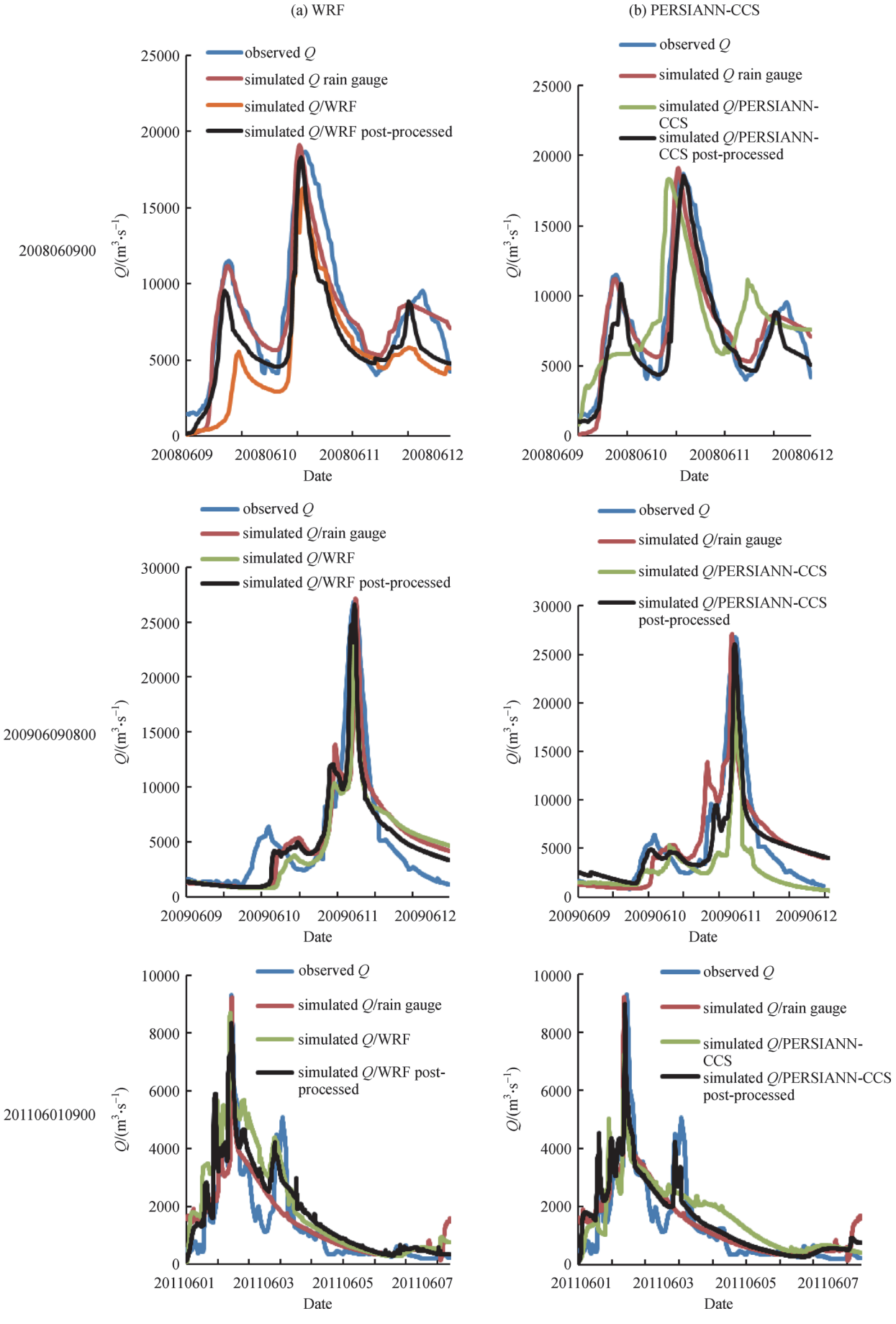
(a) WRF
(b) PERSIANN-CCS
2008060900
observed Q
simulated Q rain gauge
simulated Q/WRF
simulated Q/WRF post-processed
simulated Q/PERSIANN-CCS
simulated Q/PERSIANN-CCS post-processed
Q/(m³·s⁻¹)
Date
20080609
20080610
20080611
20080612
200906090800
simulated Q/rain gauge
simulated Q/WRF post-processed
simulated Q/PERSIANN-CCS
simulated Q/PERSIANN-CCS post-processed
20090609
20090610
20090611
20090612
201106010900
simulated Q/WRF post-processed
20110601
20110603
20110605
20110607

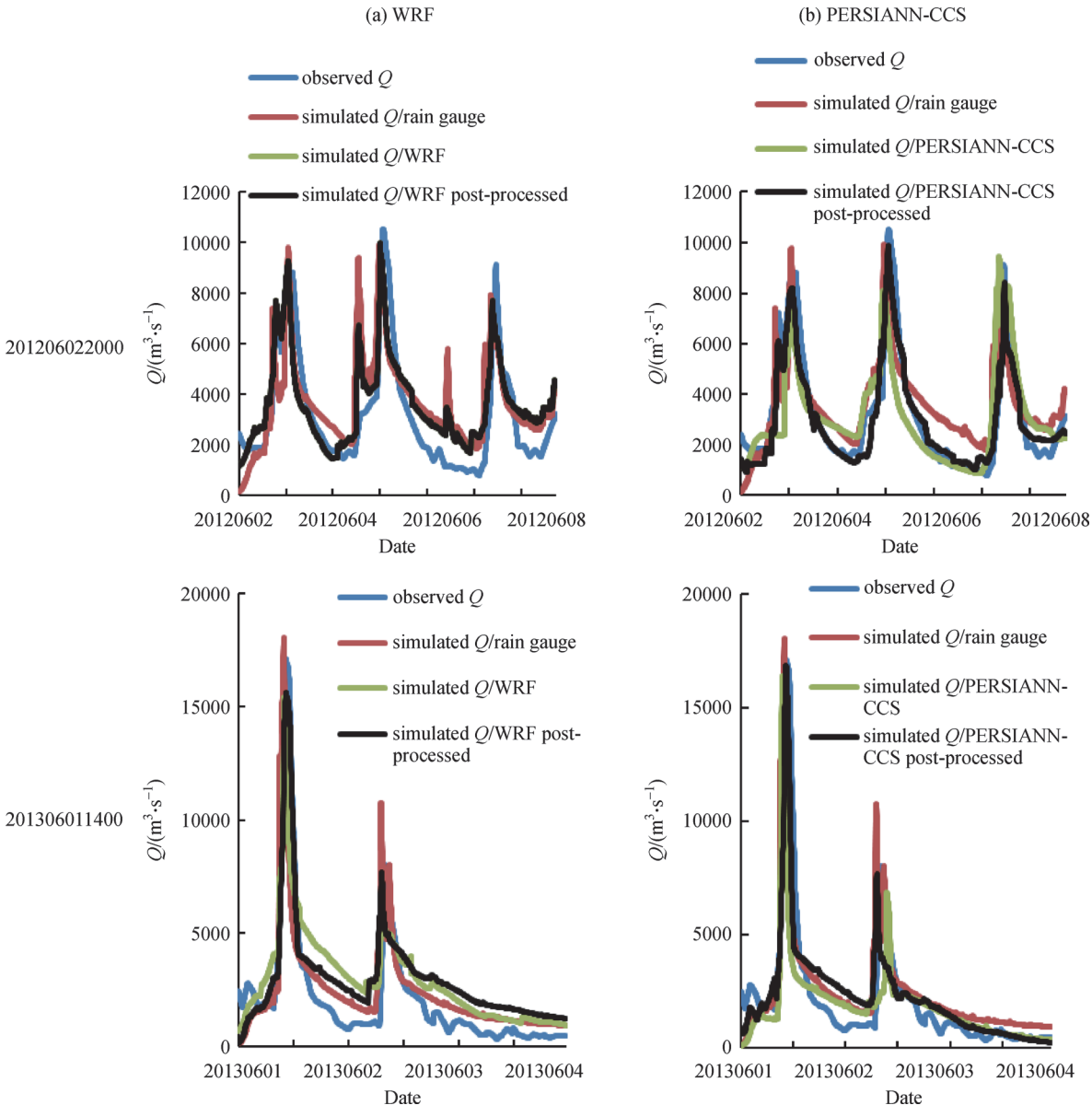

Fig. 6 The flood simulation results of flood based on the coupled model.

flows. In contrast, the coupled model performance with the postprocessed WRF QPF and PERSIANN-CCS QPEs was better. The simulated flood peak errors of the post-processed weather models were effectively reduced. For further comparison, the 6 evaluation indices of the flood simulations with the original weather models and the post-processed models are shown in Table 3.

From Table 3, all 6 evaluation indices for the postprocessed WRF QPF and PERSIANN-CCS QPEs improved compared with those for the original 2 weather models. For WRF QPF, after postprocessing, the average water balance coefficient increased by 8%, the average Nash–Sutcliffe coefficient increased by 3%, and the average correlation coefficient increased by 2%. The average process relative error decreased by 5%, the average peak flow relative error decreased by 5%, and the peak flow time error decreased by 2 h. For the postprocessing PERSIANN-CCS QPEs, the average Nash–Sutcliffe coefficient increased by 5%, the average water balance coefficient increased by 4%, and the average correlation coefficient increased by 4%. The average process relative error decreased by 5%, the average peak flow relative error decreased by 6%, and the average peak flow time error decreased by 3 h. Clearly, these evaluation indices were improved following postprocessing of WRF QPF and PERSIANN-CCS QPEs, which showed that the postprocessing method used for the 2 weather models in this study was effective and necessary.

Table 3 The evaluation indices of karst flood simulations using the original WRF QPF and PERSIANN-CCS QPEs and their postprocessed values

Floods	Rainfall types	Nash–Sutcliffe coefficient (C)	Correlation coefficient (R)	Process relative error (P)/%	Peak flow relative error (E)/%	Coefficient of water balance (W)	Peak time error (T)/h
200806090000	WRF	0.72	0.8	25	18	1.02	−9
	PP-WRF	0.78	0.82	20	13	0.95	−7
	PERSIANN	0.76	0.83	21	6	0.92	−10
	PP-PERSIANN	0.83	0.88	18	5	0.94	−4
200906090800	WR	0.81	0.82	24	20	1.12	−6
	PP-WRF	0.83	0.83	20	14	1.06	−4
	PERSIANN	0.82	0.81	28	18	0.79	−6
	PP-PERSIANN	0.85	0.87	22	12	0.85	−3
201106010900	WRF	0.79	0.81	26	14	1.15	−7
	PP-WRF	0.83	0.83	20	10	1.08	−6
	PERSIANN	0.85	0.85	21	12	0.92	−8
	PP-PERSIANN	0.91	0.87	19	6	0.94	−6
201206022000	WRF	0.78	0.82	18	13	1.28	−10
	PP-WRF	0.81	0.83	10	11	1.15	−8
	PERSIANN	0.86	0.84	16	15	0.78	−7
	PP-PERSIANN	0.92	0.89	9	6	0.85	−4
201306011400	WRF	0.78	0.82	13	21	1.2	−8
	PP-WRF	0.82	0.85	9	12	1.12	−6
	PERSIANN	0.82	0.89	12	17	0.85	−5
	PP-PERSIANN	0.86	0.91	8	9	0.87	−4
average value	WRF	0.78	0.81	21	17	1.15	−8
	PP-WRF	0.81	0.83	16	12	1.07	−6
	PERSIANN	0.82	0.84	20	14	0.85	−7
	PP-PERSIANN	0.87	0.88	15	8	0.89	−4

Remarks: WRF refers to WRF QPF, PERSIANN refers to PERSIANN-CCS QPEs, PP-WRF refers to postprocessed WRF QPF, and PP-PERSIANN refers to postprocessed PERSIANN-CCS QPEs (the same applies in the following tables).

6 Discussion

6.1 Evaluation of rainfall data from WRF and PERSIANN-CCS

To quantitatively evaluate and compare the rainfall results of the 2 weather models with the rain gauge precipitation, the average precipitation of the 3 rainfall products is listed in Table 4.

According to the rainfall results listed in Table 4, some relative errors between the 2 weather models and the rain gauge precipitation cannot be ignored. The average precipitation values of WRF QPF were larger than the rain gauge precipitation, while the PERSIANN-CCS QPE values were smaller. The relative errors between PERSIANN-CCS QPEs and the precipitation measured by rain gauges were less than those between WRF QPF and the rain gauge precipitation. The rainfall estimation results according to PERSIANN-CCS had no lead time, whereas the WRF QPF model offered rainfall forecasting with a lead time of 96 h, which provided a lead time of 96 h for flood forecasting by coupling the Karst-Liuxihe model with the WRF QPF model in this study. The average relative errors were 17% and −14% (Table 4) for WRF QPF and PERSIANN-CCS QPEs, respectively. These errors are considerable relative errors and cannot be ignored. Therefore, an effective method (Section 3.3) was used to reduce these relative errors and make the rainfall results produced by the 2 weather models more credible.

It should be pointed out that compared with the WRF QPF in this study, such as rainfall observations using rain gauges, the QPEs produced by the PERSIANN-CCS have no lead time and are only suitable for flood inversion and simulation calculations after the occurrence of floods. Therefore, PERSIANN-CCS QPEs can be coupled with the Karst-Liuxihe model to simulate historical karst flood processes, while WRF QPF could be coupled with the Karst-Liuxihe model to forecast karst floods in the future.

Table 4 Quantitative rainfall comparison results of the 3 precipitation products

Floods	Type	Average precipitation /mm	Relative bias /%
200806090200	Rain gauge	1.37	
	WRF QPF	1.55	13
	PERSIANN-CCS QPEs	1.22	−11
200906090800	Rain gauge	0.74	
	WRF QPF	0.88	19
	PERSIANN-CCS QPEs	0.62	−16
201106010900	Rain gauge	0.42	
	WRF QPF	0.46	10
	PERSIANN-CCS QPEs	0.39	−7
201206022000	Rain gauge	0.78	
	WRF QPF	0.95	22
	PERSIANN-CCS QPEs	0.63	−19
201306011400	Rain gauge	0.53	
	WRF QPF	0.65	23
	PERSIANN-CCS QPEs	0.43	−20
average value	Rain gauge	0.77	
	WRF QPF	0.9	17
	PERSIANN-CCS QPEs	0.66	−14

6.2 Evaluation of flood model outputs

This study compared the outputs of different rainfall inputs on the model performance. The different types of precipitation products, i.e., rain gauge precipitation, WRF QPF and PERSIANN-CCS QPEs, were used as inputs of the Karst-Liuxihe model to simulate floods. The comparison results are shown in Table 5.

Table 5 shows that the average evaluation indices of flood simulations based on rain gauge precipitation generated the most accurate outputs, and compared with the flood modeling outputs using WRF QPF, those with the PERSIANN-CCS QPEs improved slightly. However, the rainfall estimation results from PERSIANN-CCS have no lead time, whereas WRF QPF can offer rainfall forecasting with a lead time of 96 h; hence, a lead time of 96 h for flood forecasting can be produced by coupling the Karst-Liuxihe model with WRF QPF. This lead time of the coupled model can provide a longer response time for flood warnings.

The flood detention and peak clipping output of the upstream karst depressions were considered in the coupled model calculation (Section 4.1), making the water balance calculation in the model more reasonable and reflecting the actual flood evolution process in the karst area. The average coefficients of the water balance, W, for the precipitation measured by rain gauges, WRF QPF, and PERSIANN-CCS QPEs were 0.93, 1.07, and 0.89, respectively (as shown in Table 5). The water amount was balanced in the model. The simulated average peak time error values, T, for the rain gauge precipitation, WRF QPF, and PERSIANN-CCS QPEs were −3, −6, and −4, respectively; this provided extra lead time for flood warning and forecasting. The simulated average values of the peak flow relative error, E, for the rain gauge precipitation, WRF QPF, and PERSIANN-CCS QPEs were 4%, 12%, and 8%, respectively, which were close to the observed values. These results indicated that coupling the Karst-Liuxihe model with the postprocessed WRF QPF and PERSIANN-CCS QPEs in this paper could largely improve the accuracy of karst flood simulations and forecasting.

6.3 Uncertainty analysis of the coupled model

The uncertainty of the model simulation results mainly comes from the input data, the model structure and its parameters. Accordingly, the uncertainty analysis of the coupled model in this study focused on three aspects.

1) The reliability of the model input data, which include rainfall data, karst flood events, and hydrogeological data, was ensured; among these data, rainfall data could be reliably obtained by WRF QPF and PERSIANN-CCS QPEs and were revised effectively by the postprocessing method in this study, which made the rainfall results based on the 2 weather models closer to the true rainfall results in the basin and can largely reduce their uncertainty in rainfall forecasting; the karst flood data were obtained from the local hydrology department, which has been reviewed for reliability, consistency and representativeness; and some hydrogeological data were obtained through a field survey and tracer testing (Li et al., 2019) in the study area.

2) The uncertainty of the model structure was reduced, which was achieved mainly by improving the original Liuxihe model structure and algorithm to develop the Karst-Liuxihe model in this study area. An uncertainty analysis was carried out after the improvement of the model (Li et al., 2019).

3) The uncertainty of the model parameters was evaluated. A parameter sensitivity analysis was undertaken to evaluate the uncertainty of the coupled model in terms of model parameters (Section 4.3). To analyze the parameter sensitivity more easily, a factor SI was used, which is calculated as $SI = 1 - |DS - NSC|$. The closer SI was to 1, the more sensitive the parameter. The SI values are shown in Table 6.

The value of SI for the saturated water content parameter, θ_{sat}, was the maximum value obtained from Table 6. So it was the most sensitive parameter of the

Table 5 Evaluation indices of karst flood simulations using the three precipitation products

Floods	Rainfall types	Nash–Sutcliffe coefficient (C)	Correlation coefficient (R)	Process relative error (P)/%	Peak flow relative error (E)/%	Coefficient of water balance (W)	Peak time error (T)/h
200806090000	Rain gauge	0.96	0.94	5	3	0.94	−3
	WRF	0.78	0.82	20	13	0.95	−7
	PERSIANN	0.83	0.88	18	5	0.94	−4
200906090800	Rain gauge	0.95	0.92	17	4	0.9	−2
	WRF	0.83	0.83	20	14	1.06	−4
	PERSIANN	0.85	0.87	22	12	0.85	−3
201106010900	Rain gauge	0.95	0.92	16	3	1.02	−7
	WRF	0.83	0.83	20	10	1.08	−6
	PERSIANN	0.91	0.87	19	6	0.94	−6
201206022000	Rain gauge	0.93	0.91	8	5	0.89	−6
	WRF	0.81	0.83	10	11	1.15	−8
	PERSIANN	0.92	0.89	9	6	0.85	−4
201306011400	Rain gauge	0.95	0.94	7	6	0.92	−4
	WRF	0.82	0.85	9	12	1.12	−6
	PERSIANN	0.86	0.91	8	9	0.87	−4
average value	Rain gauge	0.95	0.93	11	4	0.93	−3
	WRF	0.81	0.83	16	12	1.07	−6
	PERSIANN	0.87	0.88	15	8	0.89	−4

Table 6 Parameter sensitivity analysis of the coupled model

Flood	Potential evaporation (E_p)	Evaporation coefficient (λ)	Wilting percentage (C_{wl})	Saturated water content (θ_{sat})	Saturation permeability coefficient (θ_s)	Macro crack volume ratio (V)
2008060900	0.18	0.26	0.11	0.94	0.92	0.78
	Field capacity (θ_{fc})	Soil layer thickness (z)	Saturated hydraulic conductivity (K_s)	Soil coefficient (b)	Bottom slope (S_p)	Bottom width (S_w)
	0.88	0.73	0.82	0.64	0.53	0.6
	Slope roughness (n)	Channel roughness (n_1)	Depletion coefficient (ω)	Permeability coefficient (K)	Specific yield of the aquifer (χ)	Thickness of the karst aquifer (h)
	0.47	0.45	0.36	0.8	0.75	0.72

coupled model. Parameters related to the soil water content in the model were very sensitive, such as the saturated water content parameter and saturation permeability coefficient. This finding indicated that the pre-soil moisture had a great influence on the final flood simulation results of the model. However, parameters related to evaporation in the model were insensitive, for example, the evaporation coefficient, potential evaporation, and wilting percentage. This result indicated that evapotranspiration loss accounted for a small proportion of flood water and had little influence on the flood simulation results, which was consistent with the actual situation in the study area.

According to Table 6, the sequence of the parameter sensitivity of the coupled model was as follows: 1) saturated water content, θ_{sat}; 2) saturation permeability coefficient, θ_s; 3) field capacity, θ_{fc}; 4) saturated hydraulic conductivity, K_s; 5) macrocrack volume ratio, V; 6) slope of the water storage content and flow curve, K; 7) proportion of the flow, χ; 8) thickness of the epikarst zone, h; 9) soil layer thickness, z; 10) Soil coefficient, b; 11) bottom width, S_w; 12) bottom slope, S_p; 13) slope roughness, n; 14) channel roughness, n_1; 15) depletion coefficient, ω; 16) evaporation coefficient, λ; 17) potential evaporation, E_p; and 18) wilting percentage, C_{wl}.

7 Conclusions

Precipitation, as the hydrological model input data, is one of the driving factors that makes the model work smoothly. However, it is often difficult to estimate effective rainfall results in karst areas. In this paper, WRF QPF and

PERSIANN-CCS QPEs were adopted to obtain acceptable precipitation estimations for the Liujiang karst river basin. A postprocessing method was proposed to revise the rainfall products using these 2 weather models. To test the effectiveness of this revision, the Karst-Liuxihe model was coupled with the postprocessed WRF QPF and PERSIANN-CCS QPEs to simulate the floods of the Liujiang karst watershed. The following conclusions were obtained from the results of this paper.

1) The quantitative precipitation results produced by WRF QPF and PERSIANN-CCS QPEs were quite close to the rainfall data observed by rain gauges, especially concerning the rainfall distribution. However, there was a relative error between the precipitation of the weather models and the rain gauges, which was 17% for WRF QPF and −14% for PERSIANN-CCS QPEs. This finding showed that WRF QPF overestimated the precipitation values, while PERSIANN-CCS QPEs underestimated the precipitation amounts. The postprocessing method proposed in this study could largely reduce these relative errors.

2) A comparison of the karst flood event outputs simulated based on the Karst-Liuxihe model after parameter optimization and the initial model parameters revealed that those produced after parameter optimization were much better. The average values of the evaluation indices, including the Nash–Sutcliffe coefficient, the correlation coefficient, and the coefficient of water balance for the Karst-Liuxihe model, increased by 29%, 26%, and 23%, respectively. The process relative error, peak flow relative error, and peak time error decreased by 17%, 31%, and 3 h, respectively. Among these parameters, the reduction in flood peak relative error was the most obvious, and it is the factor of greatest concern in flood forecasting. The results showed that it was necessary to optimize the parameters of the distributed hydrological model, and the improved PSO algorithm selected in this study was effective.

3) Compared with the karst flood event outputs simulated based on the initial 2 weather models, the flood simulations achieved with the postprocessed WRF QPF and PERSIANN-CCS QPEs were much improved. For the postprocessed WRF QPF, the average water balance coefficient, Nash–Sutcliffe coefficient, and correlation coefficient increased by 8%, 3%, and 2%, respectively. The average peak flow relative error, process relative error and peak flow time error decreased by 5%, 5%, and 2 h, respectively. For the post-processed PERSIANN-CCS QPEs, the average water balance coefficient, Nash–Sutcliffe coefficient, and correlation coefficient were increased by 4%, 5%, and 4%, respectively. The average peak flow relative error, process relative error, and peak flow time error decreased by 6%, 5%, and 3 h, respectively. Clearly, the postprocessing method proposed in this study was effective and feasible.

4) Compared with the floods simulated using the postprocessed WRF QPF, the simulation outputs achieved with the postprocessed PERSIANN-CCS QPEs were slightly better, especially in peak flow simulation. However, the rainfall data provided by PERSIANN-CCS QPEs have no lead time, which affects the simulation and inversion after the occurrence of floods. Coupling the Karst-Liuxihe model with the WRF QPF model resulted in a lead time of 96 h in flood forecasting, which could provide an adequate amount of time for flood warnings and emergency responses. The satisfactory flood simulation results indicated that coupling the 2 weather models with the Karst-Liuxihe model in this paper was feasible and reasonable for the Liujiang karst river basin.

5) The parametric uncertainty analysis for the coupled model showed that the saturated water content parameter θ_{sat} was the most sensitive. The parameter sensitivity sequence of the Karst-Liuxihe model was as follows: 1) saturated water content, θ_{sat}; 2) saturation permeability coefficient, θ_s; 3) field capacity, θ_{fc}; 4) saturated hydraulic conductivity, K_s; 5) macrocrack volume ratio, V; 6) slope of the water storage content and flow curve, K; 7) proportion of the flow, χ; 8) thickness of the epikarst zone, h; 9) soil layer thickness, z; 10) Soil coefficient, b; 11) bottom width, S_w; 12) bottom slope, S_p; 13) slope roughness, n; 14) channel roughness, n_1; 15) depletion coefficient, ω; 16) evaporation coefficient, λ; 17) potential evaporation, E_p; and 18) wilting percentage, C_{wl}.

8 Data availability

The observed rainfall data and karst flood events were provided by the Liuzhou Hydrological Bureau, Guangxi Province, China.

The WRF model used in this study was WRF-ARW model version 3.4, and the PERSIANN-CCS QPE data can be downloaded without cost from CICS website. The Liuxihe model prototype was offered by Y Chen (Chen, 2009).

The property data of the study area, including the DEM data, the land use type, and the soil type, can be downloaded without cost. 1) The DEM data were from SRTM website. 2) The land use types can be downloaded from USGS website. 3) The soil types were from ISRIC website.

Acknowledgements This study was supported by the National Science Foundation for Young Scientists of China (No. 42101031), Chongqing Natural Science Foundation (No. cstc2021jcyj-msxm0007), the Open Project Program of Guangxi Key Science and Technology Innovation Base on Karst Dynamics (KDL & Guangxi 202009, KDL & Guangxi 202012), and the National Natural Science Foundation of China (Grant No. 41830648).

References

Ahlgrimm M, Forbes R M, Morcrette J J, Neggers R A (2016). ARM's

Impact on Numerical Weather Prediction at ECMWF, Meteorol Monogr 57: 28.1–28.13

Bartsotas N, Nikolopoulos E, Anagnostou E, Kallos G (2017). Improving satellite quantitative precipitation estimates through the use of high-resolution numerical weather predictions: similarities and contrasts between the Alps and Blue Nile region. In: EGU General Assembly Conference Abstracts, 19th EGU General Assembly, EGU 2017, Vienna, Austria

Bitew M M, Gebremichael M (2011). Evaluation of satellite rainfall products through hydrologic simulation in a fully distributed hydrologic model. Water Resour Res, 47(6): 1–11

Chapuis H, Jordan R B, Jolivet J, Paran F, Graillot D (2020). Karst–river interaction, elaboration of an indicator of the karst hydrological conditions applied to the Cèze River (Gard, France). In: Bertrand C, Denimal S, Steinmann M, Renard P, eds. Eurokarst 2018, Besançon, Advances in the Hydrogeology of Karst and Carbonate Resevoirs. Cham: Springer: 77–81

Chen Y B (2009). Liuxihe Model. Beijing: China Science and Technology Press

Chen Y, Zhou H, Zhang H, Du G, Zhou J (2015). Urban flood risk warning under rapid urbanization. Environ Res, 139(5): 3–10

Chen Y, Li J, Xu H (2016). Improving flood forecasting capability of physically based distributed hydrological models by parameter optimization. Hydrol Earth Syst Sci, 20(1): 375–392

Chen Y, Li J, Wang H, Qin J, Dong L (2017). Large watershed flood forecasting with high-resolution distributed hydrological model. Hydrol Earth Syst Sci, 21(2): 735–749

Chen Y (2018). Distributed Hydrological Models. Berlin: Springer

Choi J, Harvey J W, Conklin M H (1999). Use of multi-parameter sensitivity analysis to determine relative importance of factors influencing natural attenuation of mining contaminants. In: The Toxic Substances Hydrology Program Meeting, Charleston, South Carolina, USA

Chou M D, Suarez M J (1994). An efficient thermal infrared radiation parameterization for use in general circulation models, NASA Tech. Memo 104606, NASA: 1–92

Delrieu G, Bonnifait L, Kirstetter P E, Boudevillain B (2014). Dependence of radar quantitative precipitation estimation error on the rain intensity in the Cévennes region, France. Hydrol Sci J, 59(7): 1308–1319

Ek M B, Mitchell K E, Lin Y, Rogers E, Grunmann P, Koren V, Gayno G, Tarpley J D (2003). Implementation of Noah land surface model advances in the National Centers for Environmental Prediction operational mesoscale Eta model. J Geophys Res Atmos, 108(D22): 8851

Fan K, Duan L, Zhang Q, Shi P, Liu J, Gu X, Kong D (2017). Downscaling analysis of TRMM precipitation based on multiple high-resolution satellite data in the Inner Mongolia, China. Sci Geograph Sin, 37(9): 1411–1421

Fan Z, Hao Z, Chen Y, Wang J H, Huang F H (2012). The application and research of income flood simulation of the Baipenzhu Reservoir with the Liuxihe Model. Acta Sci Natur Univ Sunyatseni, 51(2): 113–118

Faure D, Gaussiat N, Tabary P, Urban B (2015). Real time integration of foreign radar quantitative precipitation estimations (QPEs) in the French national QPE mosaic. In: 37th Conference on Radar Meteorology, AMS, Norman, OK, USA

Ford D, Williams P W (1989). Karst Geomorphology and Hydrology. Netherlands: Springer

Gebregiorgis A S, Hossain F (2013). Understanding the dependence of satellite rainfall uncertainty on topography and climate for hydrologic model simulation. IEEE Trans Geosci Remote Sens, 51 (1): 704–718

Goudenhoofdt E, Delobbe L (2009). Evaluation of radar-gauge merging methods for quantitative precipitation estimates. Hydrol Earth Syst Sci, 13(2): 195–203

Higgins R W, Silva V B S, Shi W, Larson J (2007). Relationships between climate variability and fluctuations in daily precipitation over the United States. J Clim, 20(14): 3561

Hong S, Lim J (2006). The WRF Single-Moment 6-Class Microphysics Scheme (WSM6). Asia-Pacific J Atmos Sci, 42: 129–151

Hong Y, Gochis D, Cheng J, Hsu K, Sorooshian S (2007). Evaluation of PERSIANN-CCS rainfall measurement using the NAME event rain gauge network. J Hydrometeorol, 8(3): 469–482

Hong Y, Hsu K L, Sorooshian S, Gao X (2004). Precipitation estimation from remotely sensed imagery using an artificial neural network cloud classification system. J App Meteor, 43(12): 1834–1853

Hsu K L, Gupta, H V, Gao X G, Sorooshian S (1999). Estimation of physical variables from multichannel remotely sensed imagery using a neural network: application to rainfall estimation. Water Resourc Res, 35(5): 1605–1618

Hsu K, Braithwaite D, Imam B, Gao X, Sorooshian S (2008). Bias adjustment of PERSIANN rainfall for hydrologic applications. In: American Geophysical Union, Spring Meeting Abstracts, San Francisco, CA, USA

Hu Q F, Yang D W, Wang Y T, Yang H B, Liu Y (2013). Characteristics and sources of errors in daily TRMM precipitation product over Ganjiang River Basin in China. Adv Water Sci, 24(6): 794–800

Hui Z, Chen Y, Zhou J H (2015). Assessing the long-term impact of urbanization on run-off using a remote-sensing-supported hydrological model. Int J Remote Sens, 36(21): 1–17

Johnson C M (2014). Influence of karst landscape on weather systems: a WRF model study on responses for different land and soil types. In: 28th Conference on Hydrology, Land-Atmosphere Interactions Part III, Atlanta, GA, USA

Johnson C M, Fan X, Mahmood R, Groves C, Polk J S, Yan J (2018). Evaluating weather research and forecasting model sensitivity to land and soil conditions representative of karst landscapes. Boundary-Layer Meteor, 166: 1–28

Kain J S (2004). The Kain–Fritsch convective parameterization: an update. J Appl Meteorol Climatol, 43(1): 170–181

Kovacs A, Perrochet P (2011). Hydrograph analysis for parameter estimation of connected and karst systems. In: Proceedings of the 34th World Congress of the International Association for Hydro-Environment Research and Engineering: 33rd Hydrology and Water Resources Symposium and 10th Conference on Hydraulics in Water Engineering, Engineers Australia, Neuchatel, Switzerland

Lahmers T M (2017). Enhancements to the WRF-Hydro hydrologic model structure for semi-arid environments. In: American Geophysical Union, Fall Meeting Abstracts, New Orleans, USA

Leeper R, Mahmood R, Quintanar A I (2011). Influence of karst landscape on planetary boundary layer atmosphere: a weather

research and forecasting (WRF) model-based investigation. J Hydrometeorol, 12(6): 1512–1529

Li J, Chen Y, Wang H, Qin J, Li J, Chiao S (2017). Extending flood forecasting lead time in a large watershed by coupling WRF QPF with a distributed hydrological model. Hydrol Earth Syst Sci, 21(2): 1279–1294

Li J, Yuan D, Liu J, Jiang Y, Chen Y, Hsu K L, Sorooshian S (2019). Predicting floods in a large karst river basin by coupling PERSIANN-CCS QPEs with a physically based distributed hydrological model. Hydrol Earth Syst Sci, 23(3): 1505–1532

Li J, Hong A, Yuan D, Jiang Y, Deng S, Cao C, Liu J (2020). A new distributed karst-tunnel hydrological model and tunnel hydrological effect simulations. J Hydrol (Amst), 593: 125639

Li J, Hong A, Yuan D, Jiang Y, Zhang Y, Deng S, Cao C, Liu J, Chen Y (2021). Elaborate simulations and forecasting of the effects of urbanization on karst flood events using the improved Karst-Liuxihe Model. Catena, 197: 104990

Li Y, Lu G H, Wu Z Y, Shi J (2015). Study of a dynamic downscaling scheme for quantitative precipitation forecasting, In: Remote Sensing and GIS for Hydrology and Water Resources. Proc. IAHS, 368: 108–113

Mekonnen G, Hossain F (2010). Satellite Rainfall Applications for Surface Hydrology. Netherlands: Springer

Mlawer E J, Taubman S J, Brown P D, Iacono M J, Clough S A (1997). Radiative transfer for inhomogeneous atmospheres: RRTM, a validated correlated-K model for the longwave. J Geophys Res Atmos, 102(D14): 16663–16682

Molteni F, Buizza R, Palmer T N, Petroliagis T (1996). The ECMWF ensemble prediction system: methodology and validation. Q J R Meteorol Soc, 122(529): 73–119

Moradkhani H, Hsu K, Hong Y, Sorooshian S (2006). Investigating the impact of remotely sensed precipitation and hydrologic model uncertainties on the ensemble streamflow forecasting. Geophys Res Lett, 33(12): L12401

Nguyen P, Thorstensen A, Sorooshian S, Zhu Q, Tran H. Ashouri H (2017). Evaluation of CMIP5 model precipitation using PERSIANN-CDR. J Hydrometeor, 18: JHM-D-16–0201.1

Rafieei N A, Norouzi A, Kim B, Seo D (2014). Fusion of multiple radar-based quantitative precipitation estimates (QPE) for high-resolution flash flood prediction in large urban areas. In: AGU Fall Meeting Abstracts, AGU Fall Meeting, San Francisco, CA, USA

Scanlon B R, Mace R E, Barrett M E, Smith B (2003). Can we simulate regional groundwater flow in a karst system using equivalent porous media models? Case study, Barton Springs Edwards aquifer, USA. J Hydrol (Amst), 276(1–4): 137–158

Shuster E T, White W B (1971). Seasonal fluctuations in the chemistry of lime-stone springs: a possible means for characterizing carbonate aquifers. J Hydrol (Amst), 14(2): 93–128

Skamarock W C, Klemp J B, Dudhia J, Gill D O, Barker D M, Duda G, Huang X, Wang W, Powers J G (2008). A Description of the Advanced Research WRF Version 3. NCAR Technical Note, NCAR/TN-468, STR. National Center for Atmospheric Research, Boulder, CO, Mesoscale and Microscale Meteorology Div, Denver, Colorado, USA

Sorooshian S, Hsu K L, Gao X, Gupta H V, Imam B, Braithwaite D (2000). Evaluation of PERSIANN system satellite-based estimates of tropical rainfall. Bull Am Meteorol Soc, 81(9): 2035–2046

Stenz R D (2014). Improving Satellite quantitative precipitation estimates by incorporating deep convective cloud optical depth. Dissertations for Master's Degree. Grand Forks: University of North Dakota

Takenaka H, Nakajima T Y, Higurashi A, Higuchi A, Takamura T, Pinker R T, Nakajima T (2011). Estimation of solar radiation using a neural network based on radiative transfer. J Geophys Res, 116(D8): D08215

Tingsanchali T (2012). Urban flood disaster management. Procedia Eng, 32: 25–37

Tong K, Su F, Yang D, Hao, Z (2014). Evaluation of satellite precipitation retrievals and their potential utilities in hydrologic modelling over the Tibetan Plateau. J Hydrol, 519: 423–437

Wardhana A, Pawitan H, Dasanto B D (2017). Application of hourly radar-gauge merging method for quantitative precipitation estimates. In: IOP Conference Series: Earth Environ Sci, 58(1): 012033, IOP Publishing

White W B (2002). Karst hydrology: recent developments and open questions. Eng Geo, 65(2–3): 85–105

White W B, White E L (2005). Ground water flux distribution between matrix, fractures, and conduits: constraints on modelling. Speleogen Evol Karst Aquifers, 3(2): 1–6

White W B (2007). A brief history of karst hydrogeology: contributions of the NSS. J Caves Karst Stud, 69(1): 13–26

Williams P W (1978). Karst research in China. Beijing: Science Press

Yang P H, Luo J Y, Peng W, Xia K S, Lin Y S (2008). Application of online technique in tracer test-a case in Qingmuguan subterranean river system, Chongqing, China. Carsologica Sinica, 27(3): 215–220 (in Chinese)

Yáñez-Morroni G, Gironás J, Caneo M, Delgado R, Garreaud R (2018). Using the weather research and forecasting (WRF) model for precipitation forecasting in an andean region with complex topography. Atmosphere, 9(8): 304–327

Zappa M, Beven K J, Bruen M, Cofiño A S, Kok K, Martin E, Nurmi P, Orfila B, Roulin E, Schröter K, Seed A, Szturc J, Vehviläinen B, Germann U, Rossa A (2010). Propagation of Uncertainty from observing systems and NWP into hydrological models: COST-731 Working Group 2. Atmos Sci Lett, 11(2): 83–91

Zaripov R B, Martynova Y V, Krupchatnikov V N, Petrov A P (2016). Atmosphere data assimilation system for the siberian region with the wrf-arw model and three-dimensional variational analysis WRF 3D-VAR. Russ Meteorol Hydrol, 41(11–12): 808–815

Zheng B R, Lan Z Y (2019). How beautiful is the karst in Southern China? The article was drawn in wechat official account: Institute for Planets